Journal of Alloys and Compounds 362 (2004) 206–217

www.elsevier.com/locate/jallcom

First experiments at the Swiss Light Source Materials Science beamline powder diffractometer

F. Gozzo [a,*], B. Schmitt [a], Th. Bortolamedi [a], C. Giannini [b], A. Guagliardi [b], M. Lange [a], D. Meister [a], D. Maden [a], P. Willmott [a], B.D. Patterson [a]

[a] *Swiss Light Source, Paul Scherrer Institute, CH-5232 Villigen PSI, Switzerland*
[b] *Institute of Crystallography (IC-CNR), c/o Dipartimento Geomineralogico, University of Bari, Via Orabona 4, 70125 Bari, Italy*

Received 6 September 2002; received in revised form 28 October 2002; accepted 6 November 2002

Abstract

The Materials Science beamline at the Swiss Light Source saw 'first light' in Spring 2001 and is presently undergoing commissioning and pilot experiment operation. In this article we concentrate on one of the three MS beamline stations, the Powder Diffractometer, and report on resolution tests and first experimental results. Using the high-resolution multi-crystal analyzer detector, full widths at half maximum (FWHM) smaller than 0.01° were measured with standard powders and FWHMs smaller than 0.003° were measured with a single Si(111) crystal and a very low-divergent incident beam. With the same detector, first residual stress measurements on low pressure plasma sprayed coatings were performed. Dynamic electric field-induced strain effects in relaxor perovskite crystals and the influence of water-soluble polymers on the early hydration of cement were studied using a fast read-out multistrip solid-state detector.

Keywords: Synchrotron radiation; X-ray diffraction; Thin films; Strain

---

1. Introduction

The Powder Diffraction end station is one of the three experimental stations at the Swiss Light Source Materials Science (MS) beamline [1]. The beamline has a minigap wiggler source and is designed to deliver a high intensity beam of hard X-ray photons (5–40 keV) to one of the following stations:

- X-ray Tomography Microscopy 32 m from the source;
- Powder Diffraction at 36 m;
- Surface Diffraction at 41 m.

Fig. 1 shows the MS beamline optics consisting of a minigap wiggler followed by a vertically collimating mirror, a double-crystal monochromator with sagittal (horizontal) focusing and a second vertically focusing mirror.

In this article we describe the powder diffraction experimental station and report on preliminary experimental results. A description of the powder diffractometer and its two independent detection systems precedes the presentation and discussion of the results.

2. The Materials Science powder diffractometer

The MS powder diffractometer consists of three coaxial heavy-duty rotation tables mounted on a lifting table, which allows a vertical motion of 1000 mm in 2 μm steps. A similar table provides support for various sample environments (e.g. a cryostat or a furnace). The central rotation table (ω-axis) hosts the sample or sample environment. Depending on the experiment, a Eulerian cradle, a spinner for powder or a spinner for flat plate samples can be mounted. The Eulerian cradle provides two additional angular movements allowing single-crystal orientation, reflectivity studies and stress measurements in the Ψ-tilting geometry [2]. The other two rotation tables contain two independent detection systems:

- a multi-crystal analyzer detector for high angular resolution (better than 0.005°);

---

* Corresponding author.
E-mail address: fabia.gozzo@psi.ch (F. Gozzo).

0925-8388/$ – see front matter © 2003 Elsevier B.V. All rights reserved.
doi:10.1016/S0925-8388(03)00585-1

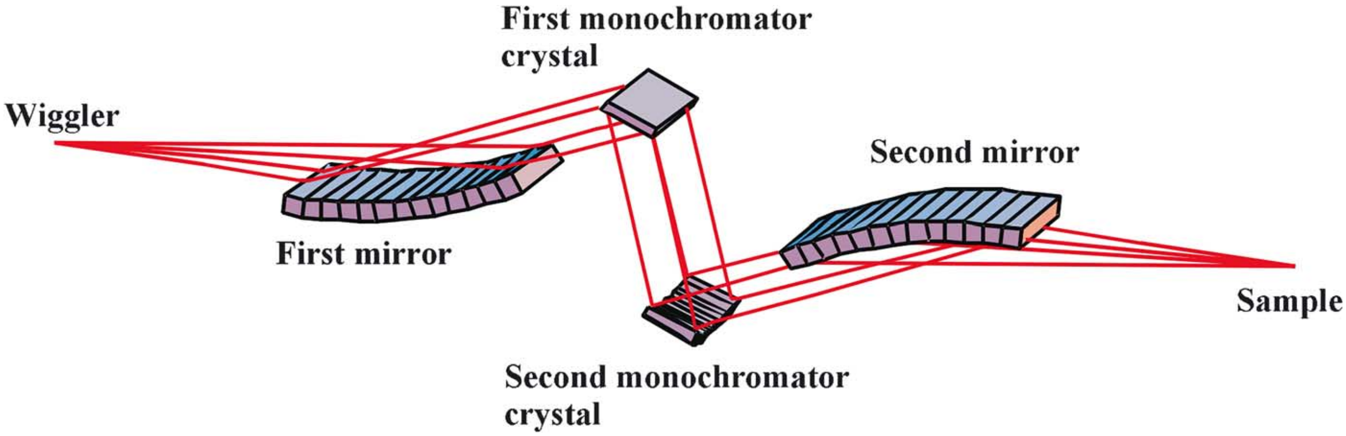

Fig. 1. Materials Science Beamline optics consisting of a wiggler source (not shown), a vertical collimating mirror, a double-crystal monochromator and a second vertically focusing mirror.

- a wide-angle (60° in 2θ), silicon microstrip detector for high-speed (sub-ms) data acquisition at angular resolution better than 0.02°.

2.1. The multi-crystal analyzer detector

High-resolution studies, such as crystallographic investigations or microstructure determinations, require both high energy and high angular resolution, since both contributions directly influence the diffraction peak line shape [3–8]. The energy resolution ($\Delta\lambda/\lambda \approx 2.0 \times 10^{-4}$ at the MS beamline) essentially depends on the quality and curvature of the first mirror (see Fig. 1) and the quality of the monochromator crystals. The angular resolution, on the other hand, depends on the residual vertical and horizontal incident X-ray beam divergence at the sample position and the intrinsic analyzer/detector angular resolution. The latter depends on the quality of the analyzer crystal (rocking curve width) and the presence of stress and curvature induced by mounting the crystals onto their mechanical support. With our Si(111) analyzer crystals, we measured rocking curves of 0.0019° at a wavelength of 1.54 Å, corresponding to the Si(111) Darwin width. The advantages of using the parallel-beam/crystal analyzer geometry (high angular resolution, independence of resolution on illuminated sample size, independence of 2θ on sample position and transparency effect and higher signal-to-noise) have been extensively described in the literature [4–6]. These advantages are obtained at the expense of the photon flux, which sometimes is so severely reduced as to make high-resolution operation feasible only when using an intrinsically collimated and intense synchrotron beam or special laboratory experimental setups (e.g. Göbel mirrors [7]). A smart solution to recover some of the lost diffracted intensity was found in 1998 by Hodeau et al. and consists of placing several independent analyzer crystals at a fixed offset, one with respect to the other, and simultaneously collecting the diffracted intensity from each of them with detectors following each crystal [8].

The analyzer crystals (five in our case) are all mounted on a θ_A–$2\theta_A$ Huber two-circle goniometer, as shown in Fig. 2. The θ_A-axis goniometer plate positions the five crystals at the correct Bragg angle for any photon energy, while the $2\theta_A$-axis goniometer plate positions, as a unit, the corresponding five scintillator/photomultiplier detectors at the right $2\theta_A$ value for every photon energy. The detectors are supplied by SCIONIX (Netherlands) and consist of NaI(Tl) scintillator crystals (20 mm diameter, 2 mm thick) optically coupled to Hamamatsu R1924 photomultipliers, each of which is followed by a preamplifier (gain 30 mV/keV with 50 Ω termination).

Each analyzer crystal corresponds to a particular detector channel. Mounting the crystals at an angular offset allows one to satisfy the Bragg condition at a given incoming photon energy for all the five channels together by simply rotating the double goniometer in a 2:1 ratio. During the acquisition of a 2θ scan, the five analyzer detector channels intercept diffraction peaks one after the other, yielding independent 2θ scans. The count rate is thus increased by a factor of 5 without increasing the data acquisition time, with the only requirement of merging the data at the end of the measurement. We are presently developing software that merges the data from the five channels after dynamically correcting for the crystal offsets and keeps track point-by-point of the statistical errors.

The five Si(111) crystals have to be carefully mounted on the double goniometer and their angular offset manually adjusted to be very close to the nominal 2° value. Although the data merging process can accept arbitrary offsets, the mounting must be precise for the following reasons:

- the relative positions of the crystals on the goniometer plate have been chosen to minimize beam shadowing;
- for each photon energy, there exists an optimum crystal-to-detector distance, for which the diffracted beams hit the center of each scintillator, but only if the

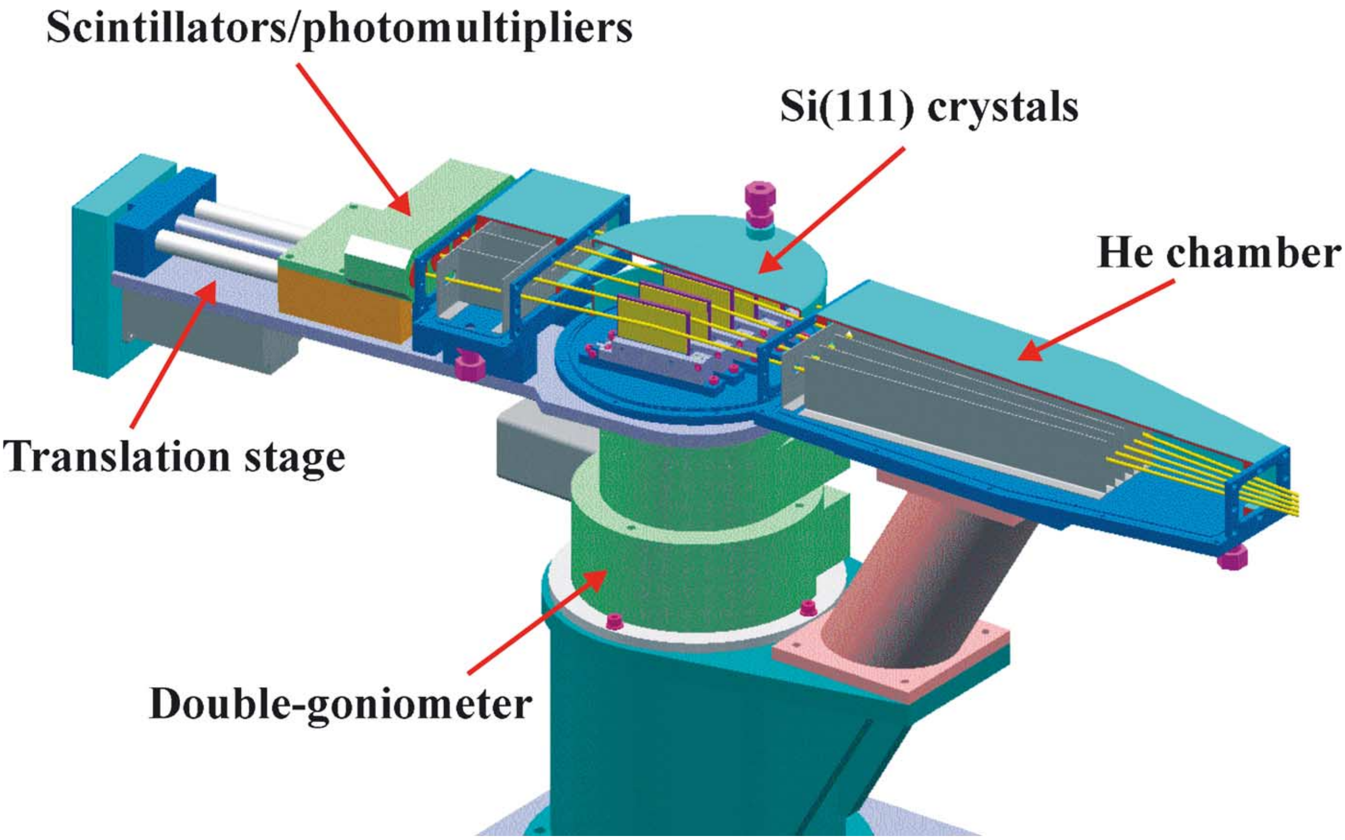

Fig. 2. High-resolution multi-crystal analyzer detector.

system of five crystals is symmetric with respect to the central crystal.

The optimum crystal-to-detector distance, as a function of the photon energy, is obtained by translating the scintillators along a translation stage, as shown in Fig. 2. The optimum distance values as a function of energy were determined graphically and the setup of the correct distance for any photon energy is presently part of routine operation.

2.2. The microstrip detector

Using the high-resolution multi-crystal analyzer detector, full diffraction patterns are obtained through 2θ scans. Although the data acquisition using five (or more) crystal analyzers in parallel considerably improves the signal-to-noise ratio without increasing the total required time, the acquisition time for high-resolution full patterns still remains of the order of hours. For time-resolved experiments, this time scale is prohibitive. A vast improvement in time-resolved powder diffractometry can be achieved by using the combination of a parallel X-ray detection system and a fast read-out, where the number of parallel detectors is now 3000 times larger than the multi-crystal analyzer [9].

The MS beamline powder diffraction microstrip detector, designed by one of the authors (B.S.), consists of 12 modules, each having 1280 independent channels, for a total of 15 360 channels. The readout time of the entire detector is 250 μs. Fig. 3 shows a schematic representation of the microstrip setup. A single detector module is entirely contained on a small printed circuit board, the MCB (Module Circuit

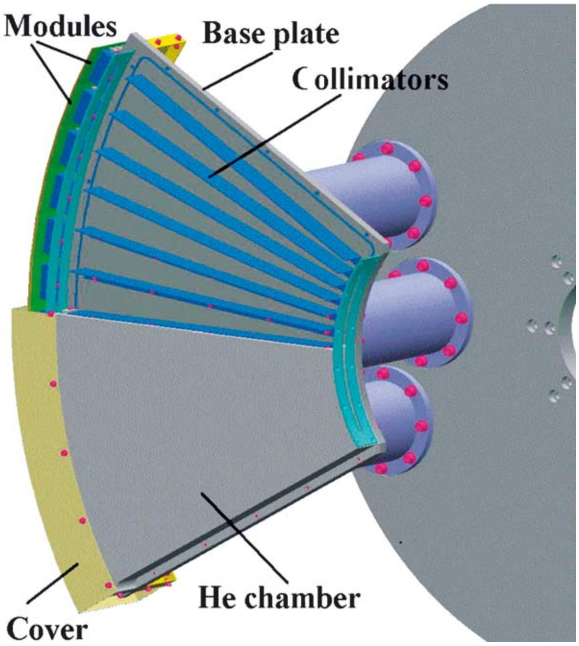

Fig. 3. Microstrip detector setup for time-resolved powder diffractometry.

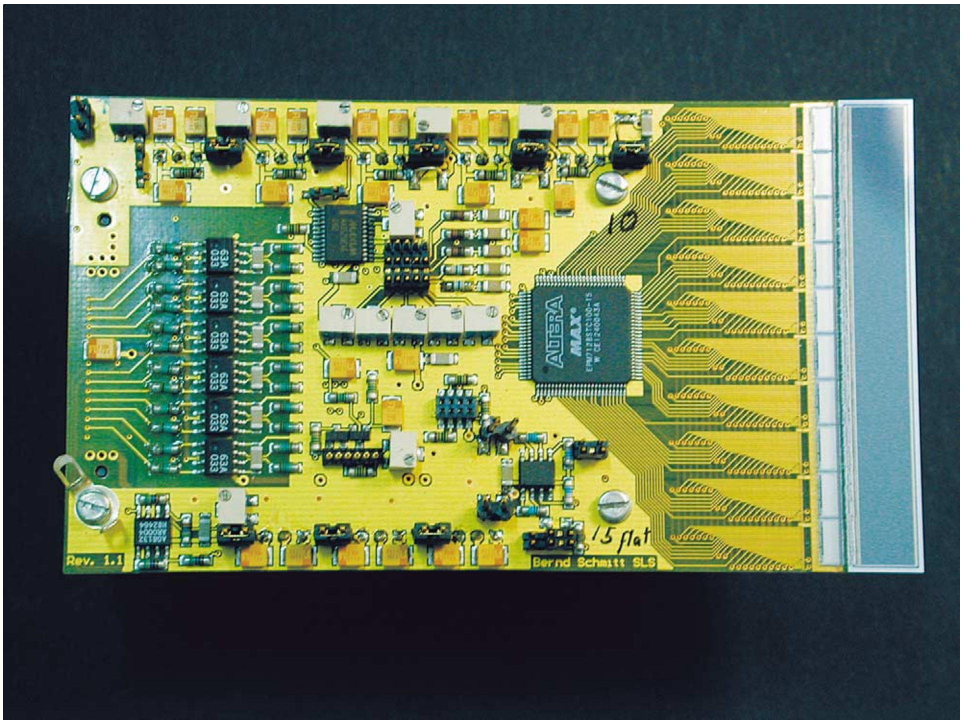

Fig. 4. Microstrip Module Control Board (MCB).

Board), shown in Fig. 4. From right to left in the figure one sees the silicon sensor, followed by 10 readout chips connected to the Si sensor by wire bonding. The 300 μm thick sensor consists of 1280 strips, each 8 mm long with a pitch of 50 μm, and each readout chip has 128 independent channels, for a total of 1280 independent channels, one for each sensor strip. X-ray photons arrive onto the Si sensor, consisting of 1280 Si p–n junctions with Al contacts. The distance between neighboring strips (pitch) defines the effective size of the strips. Electron–hole pairs are created by the X-ray photons and separated by a voltage applied to the junction. On average, 3.62 eV are needed to create one electron–hole pair. Therefore, in the energy range 5–40 keV at the Materials Science beamline, a charge $\{Q = [E(\text{eV})/3.62] \cdot e^{-}\}$ of approximately 1400 to 11 000 electrons is generated by an absorbed photon. Due to the dependence of absorption on photon energy, the detector efficiency, which is close to 100% up to 7 keV, drops to 15% at 25 keV.

The detector is operated in single-photon-counting mode. This means that each X-ray is counted, which generates a charge above a certain threshold. The threshold is preferably set at half the X-ray energy to avoid dead regions between strips. The noise of the chip should be several times lower than the threshold in order to avoid spurious counts. The main requirements of the readout chips are low noise and low threshold variations. Furthermore, its count rate should be larger than 1 MHz to avoid dead-time corrections due to the high flux of the synchrotron beam.

The ultimate microstrip detector angular resolution is determined by the pitch p of the strips and the sample-to-strip distance L:

$$\Delta\theta_{\text{ultimate}} = \arctan\left(\frac{p}{L}\right) = 0.004^{\circ}$$

where $p = 50$ μm and $L = 700$ mm at our diffractometer.

The ultimate microstrip angular resolution is, of course, lowered by the finite sample and/or beam size d:

$$\frac{\Delta\theta}{2} = \arctan\left(\frac{d+p}{2L}\right)$$

The angular resolution is, therefore, directly proportional to the strip pitch and the sample size (or beam size, whichever is smaller) and inversely proportional to the sample-to-strip distance. $\Delta\theta$ is, therefore, approximately 0.0122° for $d = 100$ μm and 0.0450° for $d = 500$ μm.

3. Results and discussion

We discuss in this section resolution tests and pilot experiments performed with both detectors during the first beamline and diffractometer commissioning.

3.1. Resolution tests

Optics tuning and resolution tests were performed using two standard powders from the U.S. National Institute of Standards and Technology (NIST) (Si 640c and LaB_6 660a) and a Si(111) single crystal. The latter was used to measure

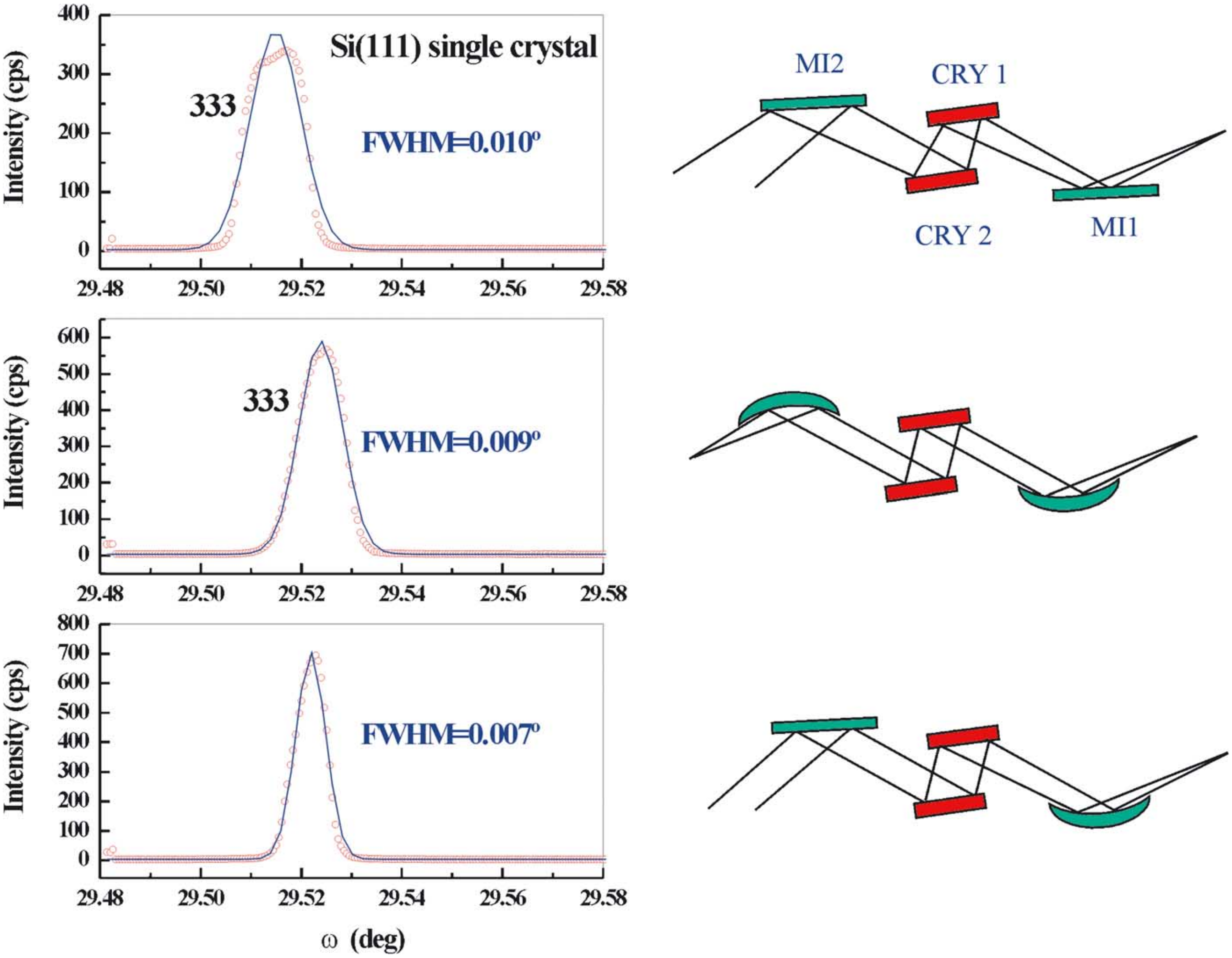

Fig. 5. Effect of mirror curvature on the energy and angular resolution. MI1 and MI2 are the first and second optics mirrors and CRY1 and CRY2 are the first and second monochromator crystals.

the broadening effect due to the divergence of the incident beam.

Fig. 5 shows the effect of mirror curvature on the energy and angular resolution. The effects on the rocking curve width of the single-crystal Si(333) Bragg reflection were observed using a wide-acceptance Si photodiode detector. The crystal was mounted on the Eulerian cradle in a dispersive configuration, in order to be sensitive to the incident beam divergence [10]. The smaller energy and angular spreads correspond, as expected, to a collimated vertical beam on the first crystal (first mirror bent) and a parallel beam at the sample position (second mirror flat).

The same crystal sample was used to test the overall resolution with the multi-analyzer detector. Fig. 6 shows ω–2θ scans of the Si (111) reflection at 12 keV. Using the front-end slits, we reduced the 0.23 mrad beam divergence of the source by factors of 30 and 80, resulting in measured FWHM linewidths of 0.0047° and 0.0025° in 2θ. The sharpest linewidth reproduces, within the accuracy of the rotation stages (±2 arcsec), the expected rocking curve width for Si(111) at this energy.

Resolution tests with powders were performed using standard powders. With the Si powder (NIST 640c), we were unable to measure (111) linewidths smaller than approximately 0.013° at 12 keV photon energy. We interpret this value as the intrinsic peak width, since it remained unchanged after tuning the beamline optics.

Using the new low-stress LaB_6 660a NIST standard powder, we were able to measure at 12 keV linewidths below 0.01° with fairly relaxed optics (beam divergence reduced only by a factor of 5 and focused beam). However, we were once again limited by the intrinsic powder sample linewidth, since flattening the second mirror produced only a decrease in flux without any reduction in linewidth.

Using the same LaB_6 standard powder, we also studied the dependence of the linewidth on 2θ, a function known as the Instrumental Resolution Function (IRF). In 1987, Sabine determined IRF analytical expressions for multi-crystal

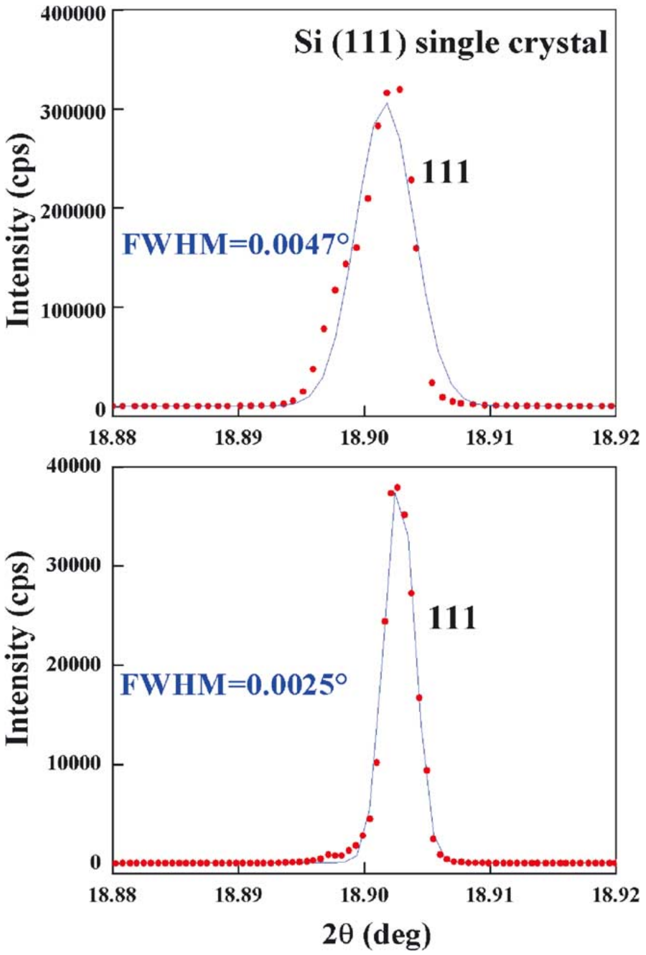

Fig. 6. ω–2θ scan of the 111 reflection from a Si(111) single crystal. The detection system used is the multi-crystal analyzer detector and the photon energy 12 keV.

spectrometers and parallel beam optics, assuming Gaussian peak line shapes [11]. In the case of a double Si(111) crystal monochromator and a Si(111) analyzer crystal in the secondary beam, Sabine's IRF analytical expression is given by

$$\mathrm{FWHM}^2(2\theta) = 4\alpha_\mathrm{m}^2\left(1-\frac{\tan\theta}{\tan\theta_\mathrm{m}}\right)^2 + \frac{1}{2}\Delta_\mathrm{m}^2\left(1-2\frac{\tan\theta}{\tan\theta_\mathrm{m}}\right)^2 + \Delta_\mathrm{a}^2$$

where α_m is the vertical divergence of the incident monochromatic beam, θ_m is the monochromator Bragg angle, Δ_m is the Darwin width of the monochromator crystal, and Δ_a is the Darwin width of the analyzer crystal.

Full diffraction patterns were recorded at 8 and 13 keV photon energies with a focused beam and experimental IRFs were determined by curve-fitting using the Rietveld method [12] implemented in the program QUANTO [13]. La and B coordinates were derived using the program EXPO [14] for ab-initio structure solution based on Direct Methods, the isotropic thermal parameters fixed at 0.2 and 0.3 for La and B, and the experimental data were corrected for Lorentz and absorption factors in the Debye–Scherrer geometry [15]. In order to take the absorption factors correctly into account, the μR values (linear absorption coefficient times the radius of the capillary containing the powder sample) were estimated experimentally ($\mu R = 0.5740$ for 13 keV) by scanning the photon beam across the sample capillary while recording the transmitted intensity. For 8 keV, the μR value was extrapolated from that measured at 13 keV, giving a value of 2.01 cm^{-1}. The background in the full patterns was described using a sixth-order polynomial.

The peak shape and width were modeled using a Pearson VII function:

$$P = \frac{C_2}{H_h}\left[1+\frac{C_3(2\theta_i-2\theta_h)^2}{H_h^2}\right]^{-m}$$

where

$$C_2 = \frac{2\Gamma(m)\sqrt{2^{1/m}-1}}{\Gamma(m-0.5)\sqrt{\pi}}$$

$$C_3 = 4\sqrt{2^{1/m}-1}$$

where Γ is the Gamma function, m is the mixing parameter defining the Gaussian and Lorentzian fractions (for $m=\infty$, the shape is Gaussian; for $m=1$, the shape is Lorentzian), $2\theta_i$ is the angular position at the ith step, $2\theta_h$ is the angular position of reflection h, and H_h is the full width at half maximum (FWHM).

Experimental and fitted curves, along with the relative differences, are plotted in Fig. 7, while the details of the curve fitting for the (210) reflection at 13 keV are shown in Fig. 8. The experimental instrumental resolution functions at 8 and 13 keV are shown in Fig. 9, while Fig. 10 shows the experimental (dotted curves) and model fit (lines) according to Sabine's equation IRFs at 13 keV. The values of α_m, Δ_m and Δ_a were refined in the fit to the experimental points. For both energies the resulting values of the residual beam divergence and the monochromator rocking curve width are slightly smaller than expected. The disagreement between the experimental points and Sabine's theoretical model observed at low 2θ angles is due to the neglect of the effects of axial divergence of the incident and diffracted beams on the peak shape, which is a questionable approximation in the case of a wiggler source.

3.2. *Residual stress measurements*

Synchrotron radiation X-ray powder diffractometry is of great relevance for the non-destructive evaluation of residual stress in materials. X-ray diffraction gives the angular position of the diffraction peaks for the material under investigation and compares them with those of the unstressed material. At a fixed monochromatic wavelength λ, the angular peak shifts $\Delta\theta$ are proportional, through the Bragg law $2d\sin\theta = n\lambda$, to the variation of the interplanar distance d

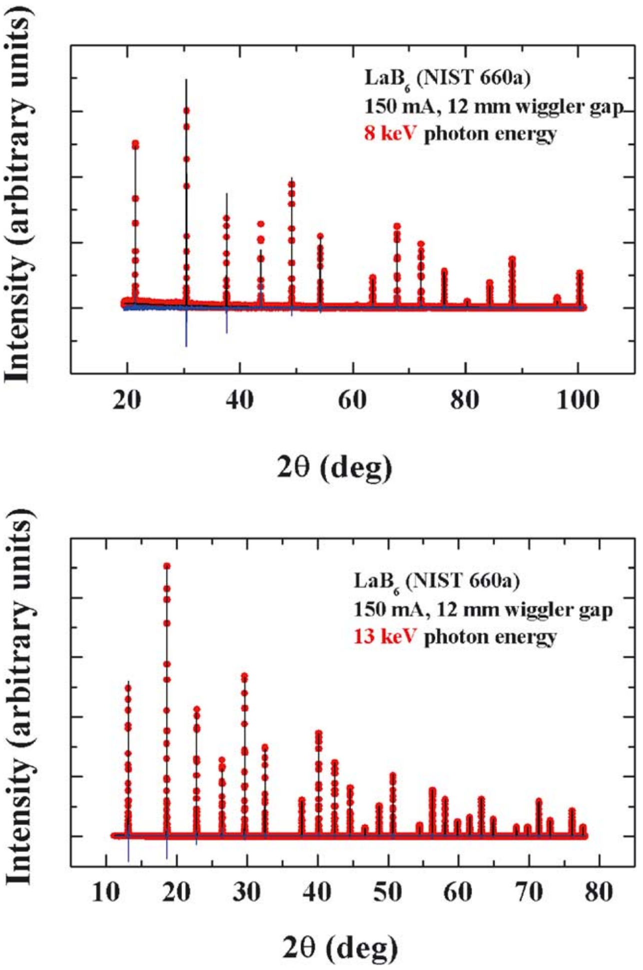

Fig. 7. Experimental and fitted LaB_6 (standard powder from the National Institute of Standard and Technology, NIST 660a) full patterns at 8 and 13 keV. The curve fitting was performed using the program QUANTO as explained in the text. The synchrotron storage ring current was 150 mA and the insertion device (wiggler) gap was 12 mm.

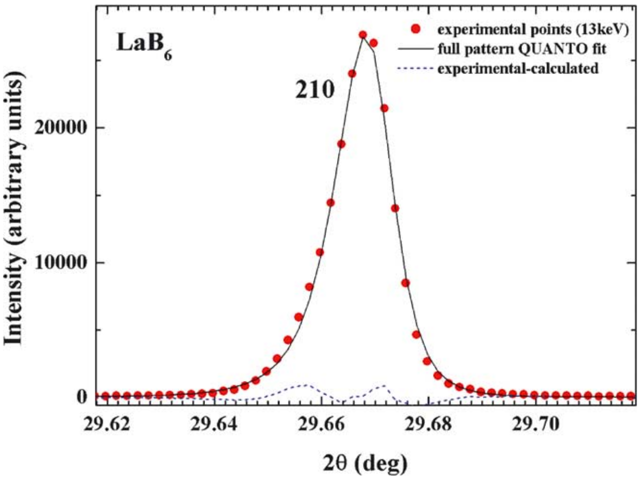

Fig. 8. Details of the full pattern curve fitting with QUANTO on the (210) reflection at 13 keV.

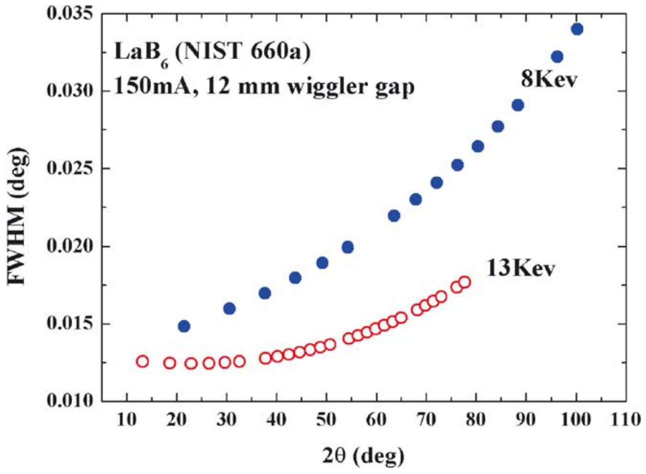

Fig. 9. Experimental instrumental resolution functions at 8 and 13 keV measured using LaB_6. The synchrotron storage ring current was 150 mA and the insertion device (wiggler) gap was 12 mm.

and, therefore, they directly probe the strain field in the material. With synchrotron radiation one profits from the tunability of the photon beam energy, which allows the study of residual stress gradients [16], and the parallel-beam/analyzer detector geometry guarantees an accurate determination of small angular shifts. At the MS beamline PD station, we are presently developing this technique for industrial applications.

Our activity in this field began approximately 2 years ago in collaboration with Sulzer Metco, a Swiss company with a world-wide recognized experience in the deposition of thin metallic and ceramic coatings using low pressure plasma spraying (LPPS) processes [17].

The main failure mechanisms in LPPS coatings are associated with the development of mechanical stresses and, in the case of ceramics, with structural instabilities. The origin of the residual stresses in plasma sprayed coatings is primarily thermal loading, both during the deposition process and

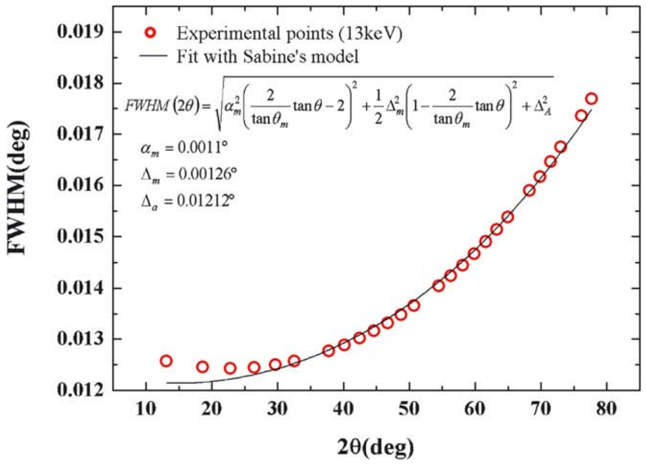

Fig. 10. Experimental IRF at 13 keV and fit to Sabine's model as explained in the text.

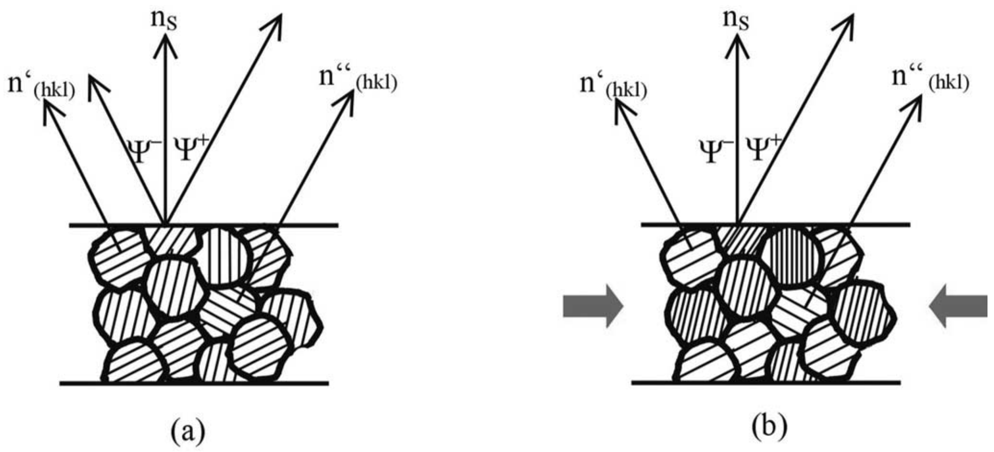

Fig. 11. Principle of the $\sin^2\Psi$ method. Measurement at positive and negative Ψ angles probes the variation of the interplanar distance d of the differently oriented grains in the polycrystal.

in service. Residual stress fields influence the formation and propagation of cracks, the delamination of the coating, shape changes and, in general, the overall performance of the mechanical part during service. Therefore, there is practical interest in optimizing the deposition parameters through stress analysis in such a way that the residual stress compensates the stress applied during service.

The X-ray diffraction approach to the evaluation of residual stresses in polycrystalline materials is the $\sin^2\Psi$ method [18]. For each selected (*hkl*) crystallographic direction, diffraction data are collected at different Ψ-tilting angles, defined as the angle between the normal to the surface and the normal to the selected crystallographic plane. Measurements at positive and negative Ψ angles probe the variation of the interplanar distance d of the differently oriented grains in the polycrystal, as shown in Fig. 11.

For biaxial stress states, randomly oriented polycrystals (i.e. no texture) and a negligible level of defects, the method predicts a linear dependence of the interplanar spacing d on $\sin^2\Psi$, with a slope proportional to the stress in the in-plane measurement direction S_Φ (see Fig. 12). When stress gradients in the direction of the surface normal S_{33} (z direction) are present ($\sigma_{ij} = \sigma_{ij}(z)$), a curvature occurs in the d vs. $\sin^2\Psi$ plots, the degree of which depends on the steepness. This 'curvature' effect is essentially due to the fact that the X-ray beam penetrates to different depths at each Ψ-tilting angle and, therefore, a different portion of the existing gradient is sampled at each Ψ angle, causing a change in the slope in the d vs. $\sin^2\Psi$ plots. When either gradients or shear stresses are non-negligible, the d vs. $\sin^2\Psi$ plots shows respectively a curvature or a split for positive and negative Ψ angles. Finally, when texture and/or defects are present, the d vs. $\sin^2\Psi$ plots show an oscillatory behavior [19].

Fig. 13 shows $\sin^2\Psi$ plots of yttria-stabilized zirconia ($ZrO_2 + Y_2O_3$) taken at 8 and 13 keV photon energies. No splitting for positive and negative Ψ angles ($\sigma_{ij} = 0$ for $i \neq j$) and no dependence on the angle Φ (azimuth) were observed, indicating an axially-symmetric uniform stress field ($\sigma_{11} \approx \sigma_{22}$). Furthermore, for LPPS coatings, the assumption can be made of a negligible stress component in the direction perpendicular to the surface ($\sigma_{33} \approx 0$). A departure from linear behavior at high ψ tilting angles was observed, indicating the presence of stress gradients, $\sigma_{ij} = \sigma_{ij}(z)$, in the S_{33} (or z) direction. When the residual

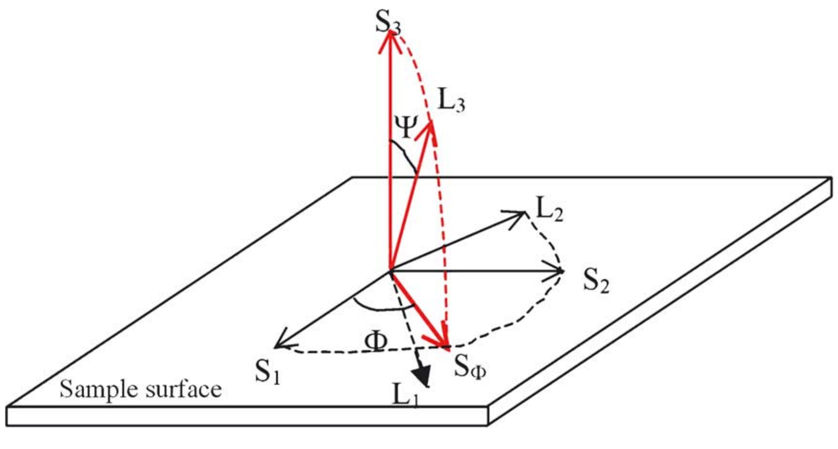

Fig. 12. Definition of the sample (S_{ij}) and laboratory (L_{ij}) reference systems [18].

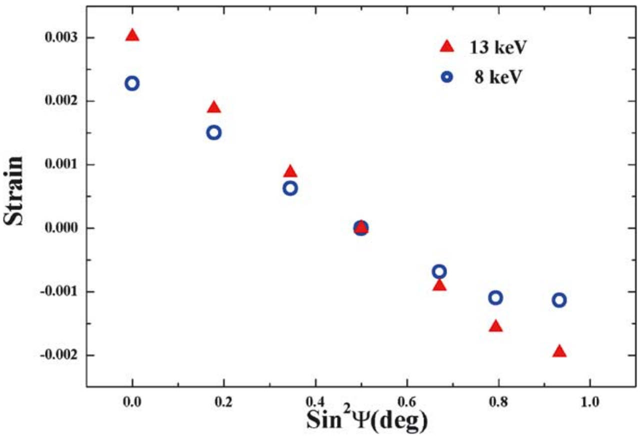

Fig. 13. $\mathrm{Sin}^2\Psi$ plots at 8 and 13 keV of low pressure plasma sprayed yttria-stabilized zirconia ($ZrO_2 + Y_2O_3$).

stress only depends on the distance z from the sample surface (in-depth gradients), we write for the averaged strain and stress in the sampled volume [20]:

$$\begin{aligned}(\varepsilon'_{33})_{\phi\psi}(hkl,\tau) &= \frac{\int_0^D (\varepsilon'_{33})_{\phi\psi}(hkl,z)\cdot e^{-z/\tau}\,\mathrm{d}z}{\int_0^D e^{-z/\tau}\,\mathrm{d}z}\\ &= \frac{1+\nu}{E}\{\langle\sigma_{11}(\tau)\rangle\cos^2\Phi+\langle\sigma_{12}(\tau)\rangle\sin 2\Phi\\ &\quad +\langle\sigma_{22}(\tau)\rangle\sin^2\Phi-\langle\sigma_{33}(\tau)\rangle\}\sin^2\Psi\\ &\quad +\left(\frac{1+\nu}{E}\right)\langle\sigma_{33}(\tau)\rangle-\frac{\nu}{E}(\langle\sigma_{11}(\tau)\rangle\\ &\quad +\langle\sigma_{22}(\tau)\rangle+\langle\sigma_{33}(\tau)\rangle)\\ &\quad +\frac{1+\nu}{E}\{\langle\sigma_{13}(\tau)\rangle\cos\Phi\\ &\quad +\langle\sigma_{23}(\tau)\rangle\sin\Phi\}\sin 2\Psi\end{aligned}$$

and

$$\sigma_{ij}(hkl,\tau)=\frac{\int_0^D \sigma_{ij}(hkl,z)\cdot e^{-z/\tau}\,\mathrm{d}z}{\int_0^D e^{-z/\tau}\,\mathrm{d}z}$$

where D is the layer thickness and $\tau = \sin\theta\cos\psi/2\mu$ the information depth in the ψ-tilting geometry, with $\mu = \mu(\lambda)$ the linear absorption coefficient.

Observe that the X-ray diffraction measurements describe the behavior of strain and stress as a function of the information depth τ. The stress profile versus the penetration depth τ should, therefore, be converted into the stress profile versus the distance z from the sample surface [20].

The principal way of determining the residual stress (RS) field with gradients is to fix exactly by strain measurements the RS versus τ dependences and to convert it into RS versus z. The conversion is done by Laplace transformations. Assuming for $\sigma_{ij}(hkl,z)$ a power law:

$$\sigma_{ij}(hkl,z)=\sum_{n=0}^{\infty}a_n z^n = a_0 + a_1 z + a_2 z^2 + \cdots$$

and replacing this expression in the equation above, we obtain

$$\begin{aligned}\sigma_{ij}(hkl,\tau) &= \frac{\int_0^D \sigma_{ij}(hkl,z)\cdot e^{-z/\tau}\,\mathrm{d}z}{\int_0^D e^{-z/\tau}\,\mathrm{d}z}\\ &= \frac{1}{\tau}\cdot\sum_{n=0}^{\infty}a_n n!\,\tau^{n+1} = a_0 + a_1\tau + 2a_2\tau^2 + \cdots\end{aligned}$$

This expression is what we obtain experimentally through $(\varepsilon'_{33})_{\phi\psi}(hkl,\tau)$. Note that the observed non-linearity in the $\sin^2\Psi$ plots is all contained in the information depth $\tau = \sin\theta\cos\psi/2\mu$.

Assuming a biaxial stress field ($\sigma_{33} \approx 0$), a linear in depth (along z) stress gradient and an axially symmetric uniform stress field ($\sigma_{11} = \sigma_{22}$), the expressions for $(\varepsilon'_{33})_{\phi\psi}(hkl,\tau)$ and $\sigma_{\phi\psi}(hkl,\tau)$ simplify as follows:

$$\sigma_{11}(hkl,\tau)=\sigma_{22}(hkl,\tau)=a_0+a_1\tau=a_0+a_1\frac{\sin\theta\cos\psi}{2\mu}$$

$$\begin{aligned}(\varepsilon'_{33})_{\phi\psi}(hkl,\tau) &= \frac{1+\nu}{E}\langle\sigma_{11}(\tau)\rangle\sin^2\Psi-\frac{2\nu}{E}\langle\sigma_{11}(\tau)\rangle\\ &= \left[\left(\frac{1+\nu}{E}\right)\sin^2\Psi-\frac{\nu}{E}\right]\cdot\left[a_0+\frac{a_1\sin\theta}{2\mu}\cos\psi\right]\end{aligned}$$

The equation above for $(\varepsilon'_{33})_{\phi\psi}(hkl,\tau)$ is an analytical expression of the experimental $\langle(\varepsilon'_{33})_{\phi\psi}(hkl,\tau)\rangle$ vs. $\sin^2\psi$ curve, where the observed non-linearity is all contained in $\cos\psi$. Collecting data at a different wavelength provides a second independent equation for $(\varepsilon'_{33})_{\phi\psi}(hkl,\tau)$, which allows one to determine the values of a_0 and a_1 through a simultaneous least-square fitting of the experimental $\langle(\varepsilon'_{33})_{\phi\psi}(hkl,\tau)\rangle$ vs. $\sin^2\psi$ curves. The linear hypothesis as well as higher degrees of the power law in $\sigma(z)$ are presently being considered to model the experimental $\sin^2\Psi$ plots in Fig. 13.

3.3. Time-resolved experiments

The first two time-resolved pilot experiments performed with the PD microstrip detector were proposed by Müller et al., Hercules GmbH, Dusseldorf [21] and Colla et al., Swiss Federal Institute of Technology, Lausanne (EPFL) [22].

Müller et al. studied the influence of water-soluble polymers on the early hydration of Portland cement. Water-soluble polymers, such as cellulose ethers (CE), are presently being studied as cement additives capable of improving workability by controlling the water balance (e.g. water retention, suspension viscosity). As a side-effect, however, the presence of these polymers significantly affects the cement hydration kinetics. The advantages of the ultra-fast acquisition time of the PD microstrip detector were exploited to study the early hydration of cement in the presence of different water-soluble polymers through the observation, as a function of time, of the presence of the crystalline phases C_3A (tri-calcium aluminate), C_3S (tri-calcium silicate), gypsum, ettringite and portlandite. Ettringite and portlandite are hydration products of C_3A plus sulfate carriers and C_3S, respectively. Fig. 14 shows the diffraction patterns collected with one single detector module in a fixed position.

Data were accumulated for 1-min periods during the first hour of hardening. The development of different crystalline phases with time is clearly visible. Specifically, Müller et al. found that CEs have a specific retarding effect on C_3S hydration (portlandite phase formation) and gypsum dissolution depended on CE chemistry, whereas the hydration of C_3A (ettrangite phase formation) is not influenced by the presence of CE in a way relevant for dry mortar applications.

The second time-resolved pilot experiment, proposed by Colla et al., was a preliminary study of the static and dynamic electric field-induced strain effect in single crystals of relaxor perovskite, $Pb(Mg_{1/3}Nb_{2/3})O_3-PbTiO_3$ (PMN-PT), with ultrahigh piezoelectric coefficients [23].

Ultrahigh strain relaxor single crystals show piezoelectric coefficients more than an order of magnitude larger than conventional piezoelectric materials and are, therefore, of considerable interest from a technological and scientific point of view. Although these materials have been the subject of intense research during the last 3–4 years, many of the basic mechanisms governing their exceptional properties still remain unclear.

The static and dynamic study of their structural properties under the action of an electric field applied under different experimental conditions (e.g. electric field intensity and frequency) is expected to provide important information on the microscopic properties of these materials.

A PMN-PT (001) single crystal was mounted and aligned on the powder diffractometer Eulerian cradle. The signal from the 002 reflection was first detected using the crystal-analyzer detector, and the signal intensity was optimized as a function of the ψ-tilting angle. Then, the crystal was turned towards the microstrip detector and the signal from the 002 reflection collected by one single detector module.

The strain effects induced by the application of an electric field were first studied under static conditions. Fig. 15a shows the displacement of the 002 reflection under the application of DC voltages of 1 and 2 kV.

The dynamic electric field-induced strain effects were studied by applying a time-dependent voltage, as shown

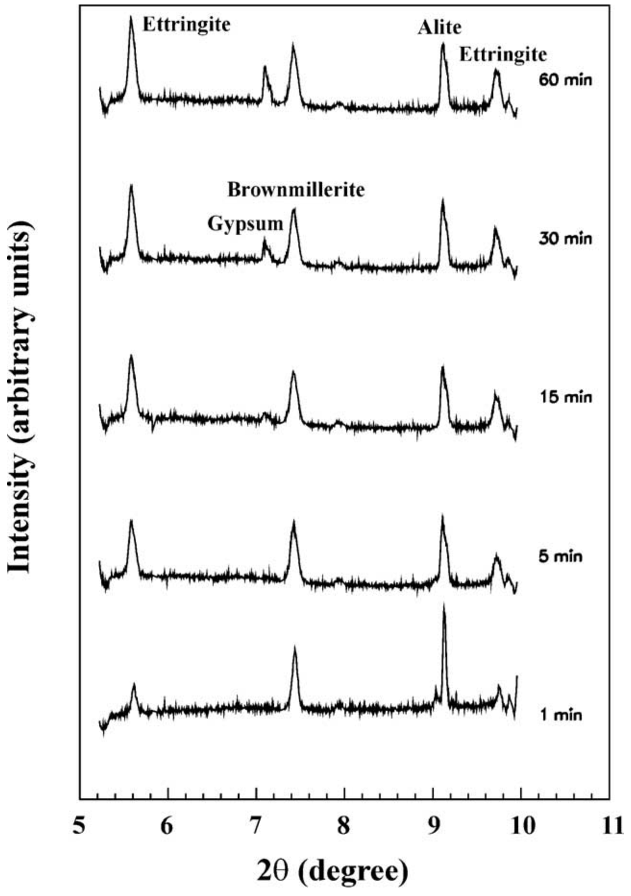

Fig. 14. Time-dependent study of the effect of water-soluble additives on the early hydration of cement.

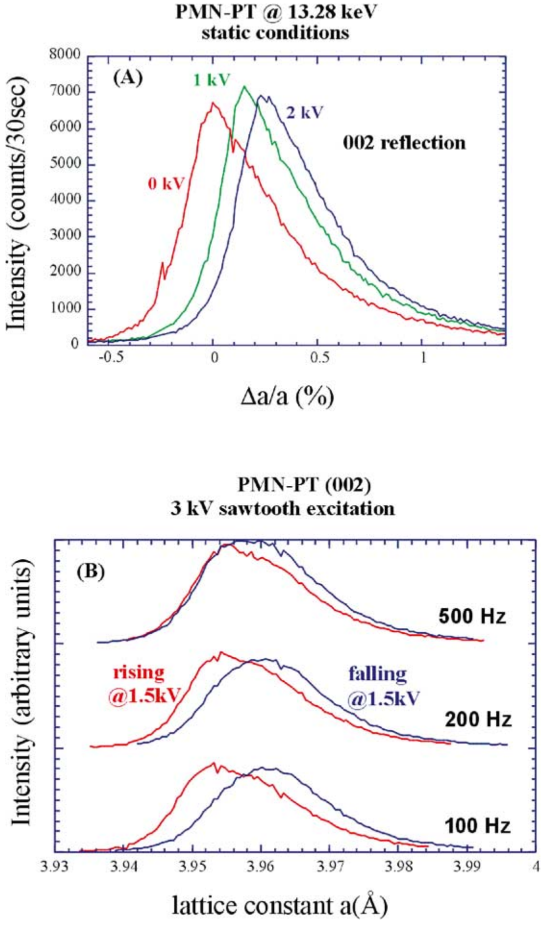

Fig. 15. Strain effects on a relaxor perovskite single crystal, induced by the application of static (a) and time-dependent (b) electric fields.

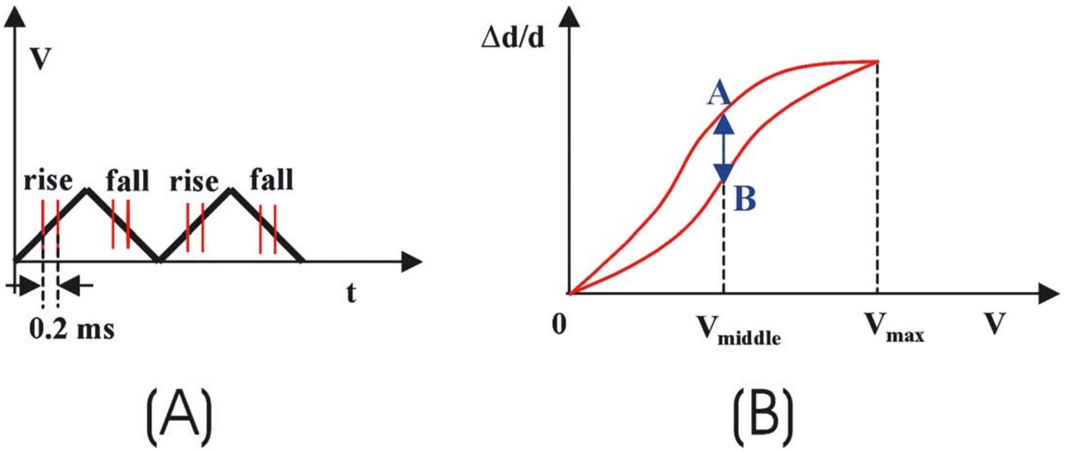

Fig. 16. Time-dependent applied voltage (a) and field-induced strain as a function of the applied voltage V (b).

in Fig. 16a (sawtooth wave excitation). The field-induced strain $\Delta d/d$ shows, as a function of the applied voltage V, the behavior described in Fig. 16b. Under dynamic conditions, the strain is expected to show a hysteresis, the magnitude of which is a function of the applied voltage frequency.

The 002 reflection was recorded at the midpoint (1.5 kV) when rising from 0 V to 3 kV and when falling from 3 kV to 0 V for a 0.2 ms interval and the measurement repeated for three frequencies (100, 200 and 500 Hz). A frequency-dependent hysteresis was clearly observed, as shown in Fig. 15b. Acquisition times of the order of ms as in the experiment described are, clearly, not possible using conventional detection systems.

4. Conclusions and future work

In this article we have described the powder diffraction station at the Swiss Light Source Materials Science beamline and, in particular, its two detection systems: the multicrystal analyzer detector for high angular resolution and the fast read-out multistrip solid-state detector for time-resolved experiments. To our knowledge, the latter is the first detector operative in synchrotron facilities. We have also discussed the most relevant resolution tests and the first experimental results.

The MS powder diffraction station is entering Phase II operation, where regular user operation alternates with periods of instrument commissioning. During commissioning time, we plan to perform a theoretical study of the beamline optics over the entire photon energy range (ray tracing) and to relate the results to the observed 2θ-dependent peak lineshape and FWHM for standard powders or single crystals. Studies of non-linear stress gradients will also be performed, and experimental determinations will be made of X-ray elastic constants using a four-point bender machine presently being installed. The microstrip detector presently works with four modules, and the installation and commissioning of the remaining eight modules is planned for this Fall.

Acknowledgements

We acknowledge the excellent work performed by F. Fauth in the design and construction phases of the SLS powder diffraction station. We thank M. Loch and G. Barbezat of Sulzer Metco for preparing samples for residual stress measurements and for fruitful discussions. We also thank E. Colla and I. Müller for kindly sharing their preliminary results with us. Finally, F.G. thanks J. Stoll for her encouragement and support.

References

[1] B.D. Patterson, R. Abela, J.F. van der Veen, Chimia 55 (2001) 534.
[2] M. Leoni, P. Scardi, in: G. Cappuccio, M.L. Terranova (Eds.), V School on X-ray Diffraction from Polycrystalline Materials, 'Thin Film Characterization by Advanced X-Ray Diffraction Techniques', October 2–5, Frascati (Rome), Italy, 1996.
[3] W.I.F. David K. Shankland, L.B. McCusker, Ch. Baerlocher (Eds.), Structure Determination From Powder Diffraction Data, IUCr Monographs on Crystallography, 2002, pp. 49–87.
[4] M. Hart, W. Parrish, Mater. Sci. Forum 9 (1986) 39–46.
[5] D.E. Cox, J.B. Hastings, W. Thomlinson, C.T. Prewitt, Nucl. Instr. Methods 208 (1983) 573–578.
[6] A.N. Fitch, Mater. Sci. Forum 228–231 (1996) 219–222.
[7] M. Gross, S. Haaga, H. Fietzek, M. Herrmann, W. Engel, Mater. Sci. Forum 278–281 (1998) 242–247.
[8] J.L. Hodeau, P. Bordet, M. Anne, A. Prat, A.N. Fitch, E. Dooryhée, G. Vaughan, A. Freund, in: Part of the SPIE Conference on Crystal and Multilayer Optics, San Diego, CA, July, 1998, SPIE Vol. 3448.
[9] B. Schmitt, Ch. Brönnimann, E.F. Eikenberry, F. Gozzo, C. Hörmann, R. Horisberger, B. Patterson (submitted for publication).
[10] D.K. Bowen, B.K. Tanner, High Resolution X-ray Diffractometry and Topography, Taylor and Francis, 1998.

[11] T.M. Sabine, J. Appl. Crystallogr. 20 (1987) 173–178.

[12] H.M. Rietveld, J. Appl. Crystallogr. 2 (1969) 65–71.

[13] A. Altomare, M.C. Burla, C. Giacovazzo, A. Guagliardi, A.G.G. Moliterni, G. Polidori, R. Rizzi, J. Appl. Crystallogr. 34 (2001) 392–397.

[14] A. Altomare, M.C. Burla, M. Camalli, B. Carrozzini, G.L. Cascarano, C. Giacovazzo, A. Guagliardi, A.G.G. Moliterni, G. Polidori, R. Rizzi, J. Appl. Crystallogr. 32 (1999) 339–340.

[15] K.D. Rouse, M.J. Cooper, E.J. York, A. Chakera, Acta Crystallogr. A 26 (1970) 682–691.

[16] P. Scardi, M. Leoni, L. Bertini, L. Bertamini, F. Cernuschi, Surf. Coat. Technol. 108/109 (1998) 93–98.

[17] M. Loch, G. Barbezat, Sulzer Techn. Rev. 2/99, 3865.

[18] I.C. Noyan, Metal. Trans. A 14A (1983) 249–258.

[19] I.C. Noyan, J.B. Cohen, Residual Stress Measurements by Diffraction and Interpretation, Springer, Berlin, 1987.

[20] V. Hauk, Structural and Residual Stress Analysis By Non-destructive Methods, Elsevier, Amsterdam, 1997.

[21] I. Müller, Hercules GmbH, Düsseldorf, Germany, private communication, 2002.

[22] E. Colla, D. Damjanovic, Swiss Federal Institute of Technology in Lausanne (EPFL), private communication, 2002.

[23] R. Guo, L.E. Cross, S.-E. Park, B. Noheda, D.E. Cox, G. Shirane, Phys. Rev. Lett. 84 (2000) 5423.